

Article

Ballistic Impact Study of an Aramid Fabric by Changing the Projectile Trajectory

Larisa Titire  and Cristian Muntenita * 

Faculty of Engineering, “Dunărea de Jos” University, 800008 Galati, Romania; larisa.chiper@ugal.ro

* Correspondence: cristian.muntenita@ugal.ro

Abstract: Personal protective systems widely use aramid textile fabrics, whether in soft or rigid form, to protect against various types of ballistic threats. Ballistic impact refers to a high-velocity impact caused by a thrusting source, often involving a low-mass object. To use these materials effectively in structural applications, it is crucial to have a thorough understanding of their ballistic behavior when subjected to high-velocity impact. Upon contact of the projectile with the ballistic material, complex ballistic penetration processes take place, which require a comprehensive and quantitative examination for a better understanding. This study aims to analyze the damage mechanism of aramid fabric by altering the projectile impact trajectory based on numerical simulations. We aim to obtain a thorough understanding of the behavior of the aramid fabric by performing numerical simulations and examining the penetration process in detail. The obtained results are analyzed based on the von Mises stress distribution (panel and projectile, projectile only, and main wires), projectile deformation, projectile velocity during ballistic impact, and based on photographs obtained during the impact.

Keywords: ballistic impact; projectile trajectory; aramid; numerical modeling



Academic Editor: Martin J. D. Clift

Received: 28 October 2024

Revised: 12 December 2024

Accepted: 8 January 2025

Published: 14 January 2025

Citation: Titire, L.; Muntenita, C. Ballistic Impact Study of an Aramid Fabric by Changing the Projectile Trajectory. *Fibers* **2025**, *13*, 8. <https://doi.org/10.3390/fib13010008>

Copyright: © 2025 by the authors. Licensee MDPI, Basel, Switzerland. This article is an open access article distributed under the terms and conditions of the Creative Commons Attribution (CC BY) license (<https://creativecommons.org/licenses/by/4.0/>).

1. Introduction

Body armor was once utilized to safeguard soldiers in conflict. In the production of body armor, the pursuit of stronger and more lightweight materials has always proven essential for enhancing performance while minimizing weight [1]. The utilization of high-performance materials for protection against ballistics has enabled the creation of fabric-based, flexible body armor that offers adequate ballistic defense, lightweight characteristics, and flexibility [2]. In addition to creating high-performance materials, concurrent efforts to comprehend their energy absorption mechanisms during ballistic impact have consistently continued. Over the past decades, researchers have studied the behavior of ballistic materials using experimental [3–8], analytical [9–11], and computational [12–18] approaches to identify the ballistic impact mechanisms that influence impact resistance.

A crucial element of an oblique impact is the modification in a projectile’s trajectory upon impact. The trajectory here refers to the angle between the bullet and the line perpendicular to the target’s surface, also known as the angle of incidence. This is also known as the angle of incidence. If a projectile impacts a target at an angle, axial symmetry is absent, and the ensuing forces do not align with its trajectory. The element of the impact that is perpendicular to the projectile’s trajectory would induce a change in its orientation. The properties of the target further complicate this phenomenon, potentially causing the projectile to deflect either toward or away from its normal trajectory [19].

When a composite target is impacted at a specific angle, stress waves are generated both through its thickness and along its length [19]. The projectile would exert force on the target. In addition to a force along the penetration route, a transverse force will be created, resulting in a change in the projectile's obliquity during the whole impact event. Thus, the trajectory of the bullet would be curved. The perforation of the target is contingent upon the projectile's starting velocity. The impact process has been categorized into two phases for ease of understanding. The first phase occurs from the moment of impact until all layers have succumbed to different failure mechanisms. The second stage begins and continues until the impact process concludes, namely when the projectile has penetrated the target. With reduced incidence impact energy, projectile perforation may be absent.

Zhang et al. [20] studied the oblique impact of two metallic laminates with a hemispherical rigid projectile at different impact angles (0° , 30° , 45° , and 60°). Through numerical simulation, they discovered that the projectile deformation at oblique impact decreases as the impact velocity increases, the projectile deviation angle decreases, the residual projectile velocity correlates with the initial velocity, and the energy absorption of the metallic laminates also correlates with the initial velocity.

Biswas et al. [21] studied the ballistic resistance of an armor system made of a 95% alumina–Kevlar 29/epoxy composite under normal and oblique impact conditions. The angle of incidence ranges from 0° to 70° in 10-degree increments, while the projectile's impact velocities vary from 220 to 1200 m/s. They found that when the angle of impact decreases below 30 degrees, when the angle of impact increases, the residual projectile velocity increases by up to 15%, concluding that in the range of 30 degrees to 45 degrees, the penetration resistance of the armor indicates a lower sensitivity to impact. When the impact angle increases above 45 degrees, the ballistic limiting velocity shows a sharp increase.

Goda [22] studied the ballistic resistance of composite E-glass targets impacted by projectiles with different nose shapes and different impact angles. The analysis was carried out by numerical simulation using the Abaqus Explicit program and was validated with literature tests. It concluded that composite E-glass targets impacted by projectiles with different nose shapes and different impact angles significantly influence the impact behavior of the target.

Iqbal et al. [23] conducted a study on the effects of sharp-nosed cylindrical projectiles on Weldox Steel targets. The projectile hit the target from several angles: 0° , 15° , 30° , 45° , and 60° . The impacted targets had two thicknesses, 1 mm and 12 mm. The 12 mm thick target exhibited approximately the same ballistic limit for the cases with an angle up to 30° ; the 1 mm thick case behaved differently, indicating a significant increase in the ballistic limit. When the projectile ricocheted, the critical angle increased with increasing impact velocity.

The aim of this study is to analyze, by numerical simulation, the impact between a meso-modeled fabric and a projectile with different impact trajectories (different angles) from 0° to 70° in 10° steps. This analysis provides a detailed understanding of the equivalent stress distribution, projectile behavior, and yarn and layer breakage mechanisms, which are crucial for optimizing the design and strength of modern ballistic materials. By using this method, this work contributes to the understanding of material behavior at oblique impact, where the dynamics of projectile–fabric interactions are complex and influenced by the impact trajectory. The meso-level simulation provides a detailed insight into how stresses propagate in the yarn structure, allowing an accurate analysis of the deformation and rupture processes. These results are valuable for the design of more effective ballistic protection equipment that is tailored to withstand a wide range of angles and conditions.

The aim of this work is to analyze, by numerical simulation, the behavior of a Twaron CT736 aramid fabric panel, CT736, subjected to projectile impacts at different angles (0 – 70°)

in order to understand the distribution of the equivalent stresses, deformation, rupture mechanisms of yarns and layers, and the interactions between them. The numerical model is validated using the experimental results from the literature for a 16-layer fabric panel subjected to normal impact. This validation provides a solid basis for extending the analyses to other impact conditions and ensures the quality and accuracy of the numerical simulation, an aspect that is frequently missing in other similar studies.

This study analyzes the oblique impacts at angles ranging from 0° to 70° in steps of 10° . This significantly extends the applicability of the results compared to the research that focuses mainly on normal impact or a limited number of angles. This paper uses a meso-level approach, which simulates each individual thread in the fabric and its interactions, allowing detailed analyses of stress propagation, yarn deformation, and the contribution of the layer to energy absorption. Unlike simulated macro-level models in the literature, this approach provides a detailed insight into the structural behavior of the fabric. To facilitate simulations at large angles, this paper reduces the number of simulated layers, optimizing computational resources while ensuring model validity. This approach allows detailed analysis for oblique impacts without compromising the quality of the results. This paper details the modes of yarn failure and investigates how stresses and strains propagate between successive layers. These analyses go beyond the level of detail found in most existing works. The choice of an impact velocity of 400 m/s, comparable to the experimentally measured values (410 m/s), represents an optimal compromise between simulation accuracy and computational resource utilization, given the tolerances inherent in experimental measurements. By integrating these elements, this paper contributes significantly to the knowledge of the performance of aramid fabrics under various impact conditions and provides essential information for optimizing the design of ballistic materials.

2. Numerical Modeling

There are three structural levels in numerical simulation identified in the literature: the micro level (fiber modeling), meso level (wire modeling), and macro level (layer modeling). In layer-level modeling, at the macro level, the geometry and waves of the wires are neglected, but the advantage is that the calculation time is lower. Nunes et al. [24] studied targets with 8 layers, 13 layers, 23 layers, and 28 layers impacted by two projectiles (a 9 mm Luger and .357 Magnum). The meso-level analysis is the most widely used because the results obtained are more accurate compared to the macro-level analysis [24]. Liu et al. [25] studied, at the meso level, the impact between the modified aramid fabric and the FMJ (full metal jacket) and FSP (fragment simulating projectile) projectiles. SOLID elements are preferred for wire-level analysis since SHELL elements do not account for the changes in wire thickness and shape. Modeling at the fiber level involves representing the fabric as a collection of parallel fibers compactly clustered in the cross-section of the wire [26–29]. This allows for the simulation of important deformation and interaction mechanisms, such as friction between fibers and yarns, fiber displacement, and fiber degradation and breakage. However, these methods are extremely demanding, which limits the analysis of short wire fragments.

The impact behavior of the aramid fabric was analyzed by numerical simulation, using ANSYS Explicit Dynamics, modeling the fabric at the meso level, at the level of the yarn considered as a homogeneous structure (Figure 1). The yarn has a length of 30 mm and a thickness of 0.31 mm, corresponding to the dimensions of the Twaron CT736 fabric (Table 1) [30]. The target panel was made of 16 and 5 layers and was impacted by a 9 mm FMJ (Full Metal Jacket) projectile with modified trajectories to investigate the impact at different angles (Figure 2). The contact conditions between the projectile and the wire, as well as between the wires, were characterized by friction. A friction coefficient of 0.3

was chosen based on previous research [31–35]. The wire and projectile geometries were discretized to the same size. The target from 5 layers and projectile were discretized into 85,255 elements with 105,983 nodes.

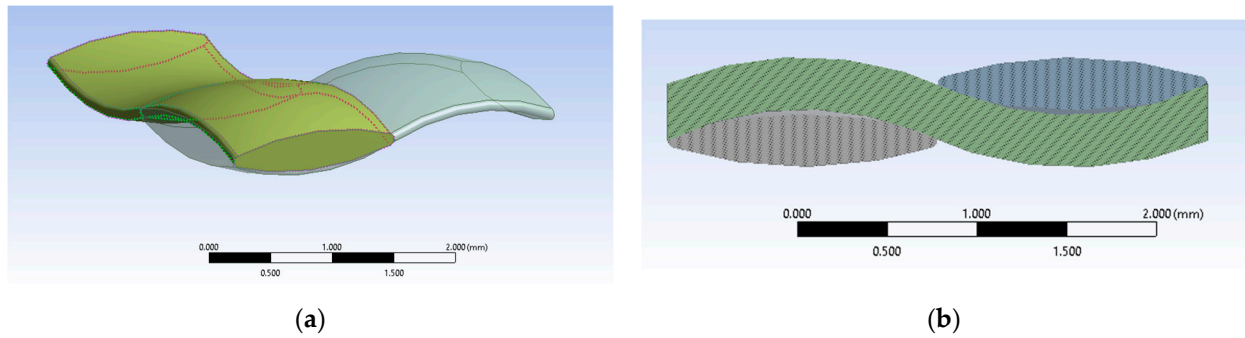


Figure 1. Geometry of the wire: (a) warp wire and weft wire; (b) cross-section and longitudinal section of the wire.

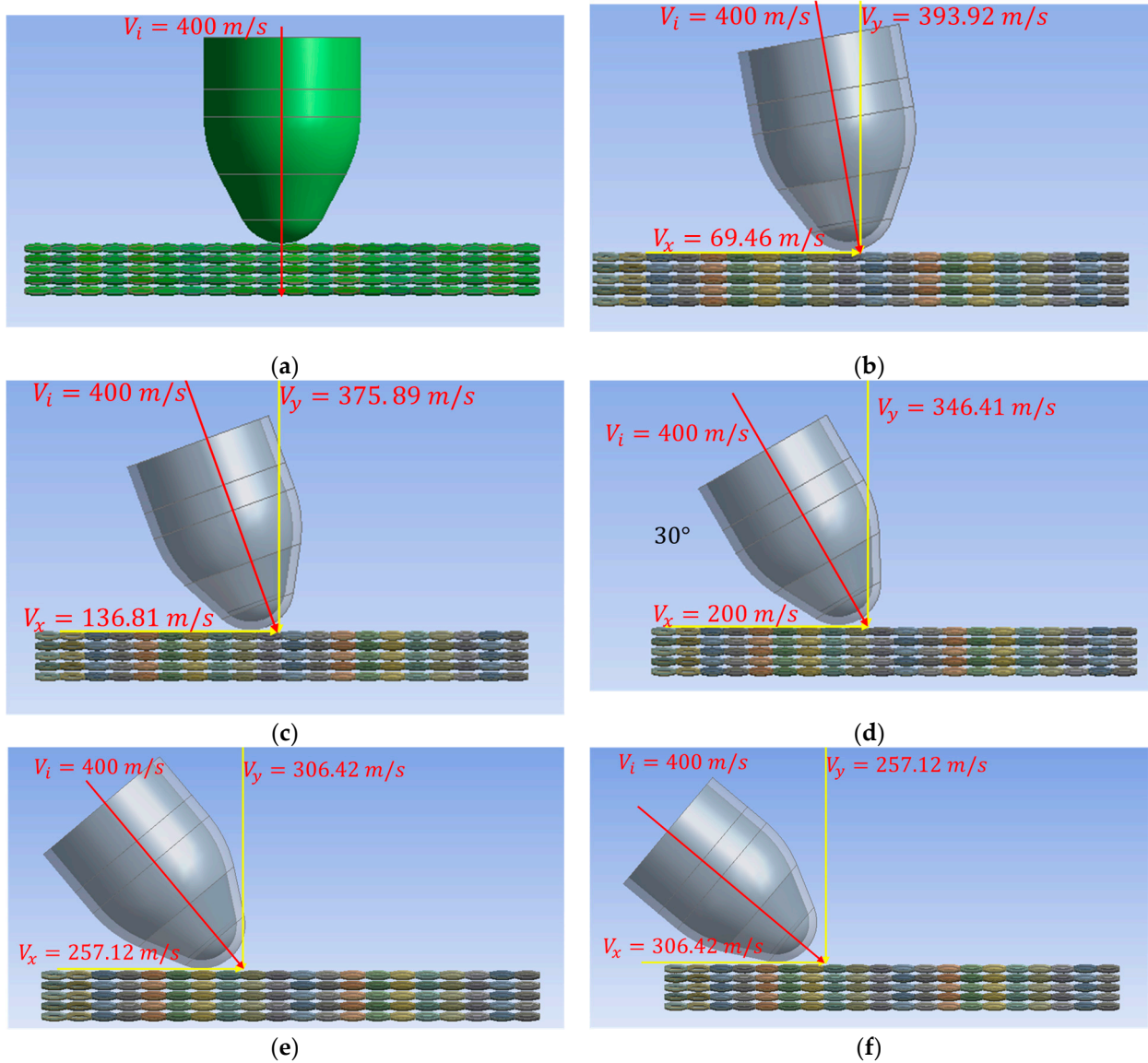


Figure 2. Cont.

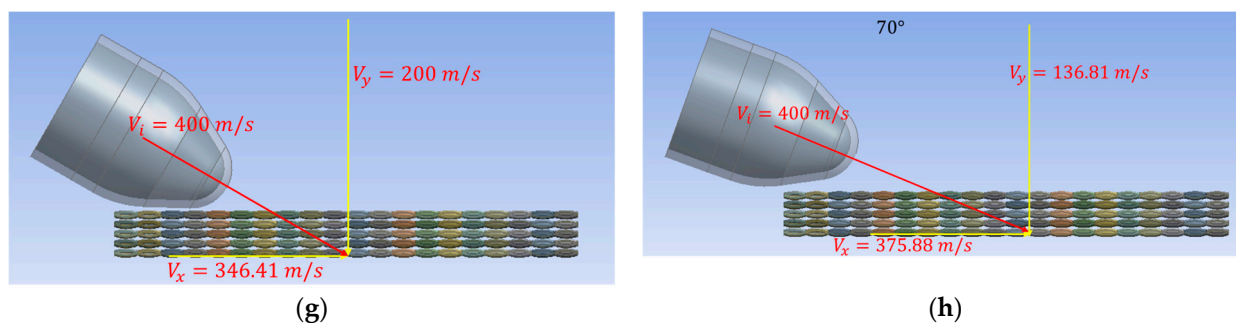


Figure 2. Components of velocity: (a) Projectile trajectory at 0°; (b) projectile trajectory at 10°; (c) projectile trajectory at 20°; (d) projectile trajectory at 30°; (e) projectile trajectory at 40°; (f) projectile trajectory at 50°; (g) projectile trajectory at 60°; and (h) projectile trajectory at 70°.

Table 1. T Properties of Twaron CT736 fabric [30].

Style	Twaron-Type	Weave	Areal Density [g/m ²]	Thickness [mm]
CT736	2000	Plain	410	0.62

The density of the simulated aramid wire is 1450 kg m⁻³, Young’s modulus is 119,000 MPa, the yield strength is 3500 MPa, and the maximum equivalent strain is 4%. These values have been selected from the literature [36–46].

The density value of the projectile jacket is 8300 kg m⁻³, Young’s modulus is 117,000 MPa, Poisson’s ratio is 0.34, the yield strength is 70 MPa, and the tangent modulus is 1150 MPa. Values for the projectile material properties were selected from the literature [47–53]. The density value of the projectile core is 11,340 kg m⁻³, Young’s modulus is 16,000 MPa, Poisson’s ratio is 0.44, and the material constants of the Johnson–Cook strength model are:

- A = 24 MPa (initial yield strength);
- B = 300 MPa (hardening constant);
- n = 1 (hardening exponent);
- c = 0.1 (strain rate constant);
- m = 1 (thermal softening exponent);
- Tm = 760 K (melting temperature);
- Reference strain rate = 1/s.

Each layer of yarn was modeled as a continuous, homogeneous structure, and the inter-yarn friction was defined to ensure realistic contact behavior. Solid elements were used for both the yarn and projectile, as they can accurately simulate volume changes, plasticity, and failure. These elements also allow for a better representation of stress–strain relationships in both the yarn and projectile materials. The initial velocity of the projectile was set to 400 m/s, simulating a typical high-velocity impact for a 9 mm FMJ projectile. The fabric panel was fixed at its edges to simulate a rigid support system. This boundary condition allowed for the simulation of a realistic dynamic response to impact.

A sufficiently small time step was chosen to capture the rapid deformation and interaction processes during the high-velocity impact. The total simulation time was set to capture the entire impact event, from initial contact to the final penetration state of the projectile.

A failure criterion based on maximum stress was applied to the yarns, which are considered to fail when the von Mises stress exceeds the material’s yield strength ($\sigma_y = 3500$ MPa). This criterion was used to identify potential failure locations within

the yarns and to track their progression through the simulation. The projectile was also modeled to undergo deformation and potential failure upon impact. The Johnson–Cook strength model was used for the projectile core material, incorporating temperature and strain rate effects to account for the plastic deformation and possible failure under high strain rates typical of ballistic impacts.

In numerical impact simulations, element erosion is triggered when the equivalent plastic strain (EPS) exceeds a critical threshold set for the aramid material. This threshold represents the plastic strain limit beyond which the material cannot return to its original shape, indicating failure or structural destruction of the element.

By using this erosion method, numerical simulations allow an accurate representation of how the aramid fabric absorbs impact energy and how the material breaks during projectile penetration. This provides a detailed understanding of the tearing and perforation formation mechanisms in aramid fabrics, providing valuable insights into the behavior of the material under extreme impact conditions.

A main wire was analyzed to identify the mode of breakage at the wire level and the von Mises stress distribution. The analyzed wire was from the first layer; the wire was in the direction of the weft (see Figure 3).

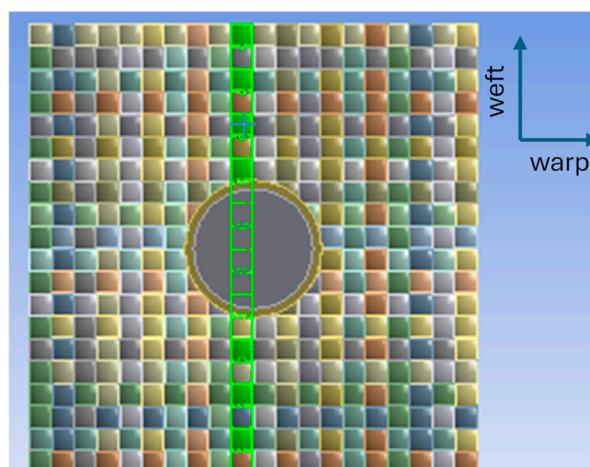


Figure 3. Main wire analyzed.

Figure 2 provides the initial impact velocities following the oblique impact. The initial velocity vector, v_i , is decomposed in the y and x directions as follows: $v_y = v_i \cos \alpha$, $v_x = v_i \sin \alpha$, where v_i represents the initial impact velocity and v_y and v_x represent the components of the impact velocity along the thickness and the surface of the target, respectively.

Description of the experimental 16-layer [54] panel tested according to NIJ 0101.06

The ballistic panel used to validate the numerical model was made of 16 layers of Twaron CT736 aramid fabric, a material known for its excellent performance in impact energy absorption and high tensile strength. The panel was made of 16 layers of fabric stacked on top of each other and stitched at the corners, ensuring the relative stability of the layers during ballistic tests.

The dimensions of the panel are 400 mm \times 400 mm, which allows a large enough area to evaluate the behavior of the material during ballistic impact. The panel was tested in accordance with the NIJ (National Institute of Justice) standard 0101.06 [55], which provides rigorous requirements for evaluating the performance of ballistic equipment.

The NIJ standard includes templates with specific contours for body armor vests by size (S, M, L, XL, and XXL), but the rectangular panel was used as an intermediate test method for material validation.

In general, for ballistic impact tests, projectile velocity is measured with high-precision equipment such as ballistic chronographs and is usually checked with a very small margin of error, but some small differences (around 1–5%) may be allowed depending on the equipment used.

Choosing the impact velocity of 400 m/s instead of 410 m/s is a practical option to optimize computational resources. The difference between the two values (about 2–3%) is very small and does not significantly influence the simulation results. Furthermore, in experimental tests, the measurement of projectile velocity using ballistic chronographs can be influenced by measurement errors inherent to this type of equipment. These natural variations in experimental measurements additionally justify the use of a rounded value, such as 400 m/s, for numerical simulation.

In the context of complex numerical simulations, where computational time and use of hardware resources are crucial factors, reducing the impact velocity to 400 m/s allows us to obtain results very close to the real ones without complicating the computational process.

Reducing the number of layers

In this research, the number of layers of the ballistic panel has been reduced for simulations for reasons related to the optimization of computational resources.

The simulation of a 16-layer panel, validated in experimental tests, at oblique impact angles (different from normal impact) would require considerable computational resources as well as a very large computational time. These requirements increase exponentially with the complexity of the model and the number of variables involved, such as the impact angle and the interactions between the layers.

Simulating impacts at oblique angles on a multi-layered panel (16 layers) can lead to a very large number of elements and interactions between layers, which makes the computational process inefficient. Reducing the number of layers allows us to explore several impact angles (10° , 20° , . . . , 70°) in a shorter time without significantly compromising the accuracy of the obtained results.

By reducing the number of layers, results relevant to the study of material behavior at oblique impacts can be obtained quickly, thus saving computational resources and time. Even if the number of layers is reduced, the main deformation and fracture mechanisms of the material are well captured, and the analysis remains valid in terms of ballistic performance.

This choice to reduce the number of layers is a balanced solution that allows valid results for oblique impact analysis without significantly sacrificing simulation accuracy or significantly increasing computational costs.

3. Results of the Numerical Simulation of the 16-Layer Panel and Model Validation

Validation of the numerical model is essential to ensure the accuracy and reliability of the simulation results. By comparing numerical data with the experimental results available in the literature, the proposed model can be evaluated both qualitatively and quantitatively. This validation step confirms that the model correctly reproduces the real behavior of the material and its response to impact. In this case, the use of a 16-layer fabric panel to simulate a normal impact provides a solid basis for comparison with established experimental work.

Validation also ensures that any subsequent analysis, such as that of the effects of varying impact angles, is based on a robust numerical model, reducing the uncertainties associated with numerical predictions. The validation process not only improves the credibility of the model but also contributes to a better understanding of the complex phenomena associated with projectile–material interactions.

Figure 4 illustrates the von Mises stress distribution for the simulated 16-layer panel made of aramid fiber strands woven in a plain weave pattern. The image highlights the formation of the projectile-induced hole, how it causes the lateral displacement of the yarns in the impact zone, and the stress distribution in the material. Localized deformation of the yarns, yarn breakage in the vicinity of the hole, as well as fragments of the yarns adhering to the projectile tip can be observed. These details indicate an intense interaction between the projectile and the fabric, characterized by complex deformation and tearing mechanisms, confirming the distinctive behavior of plain aramid weave under impact.

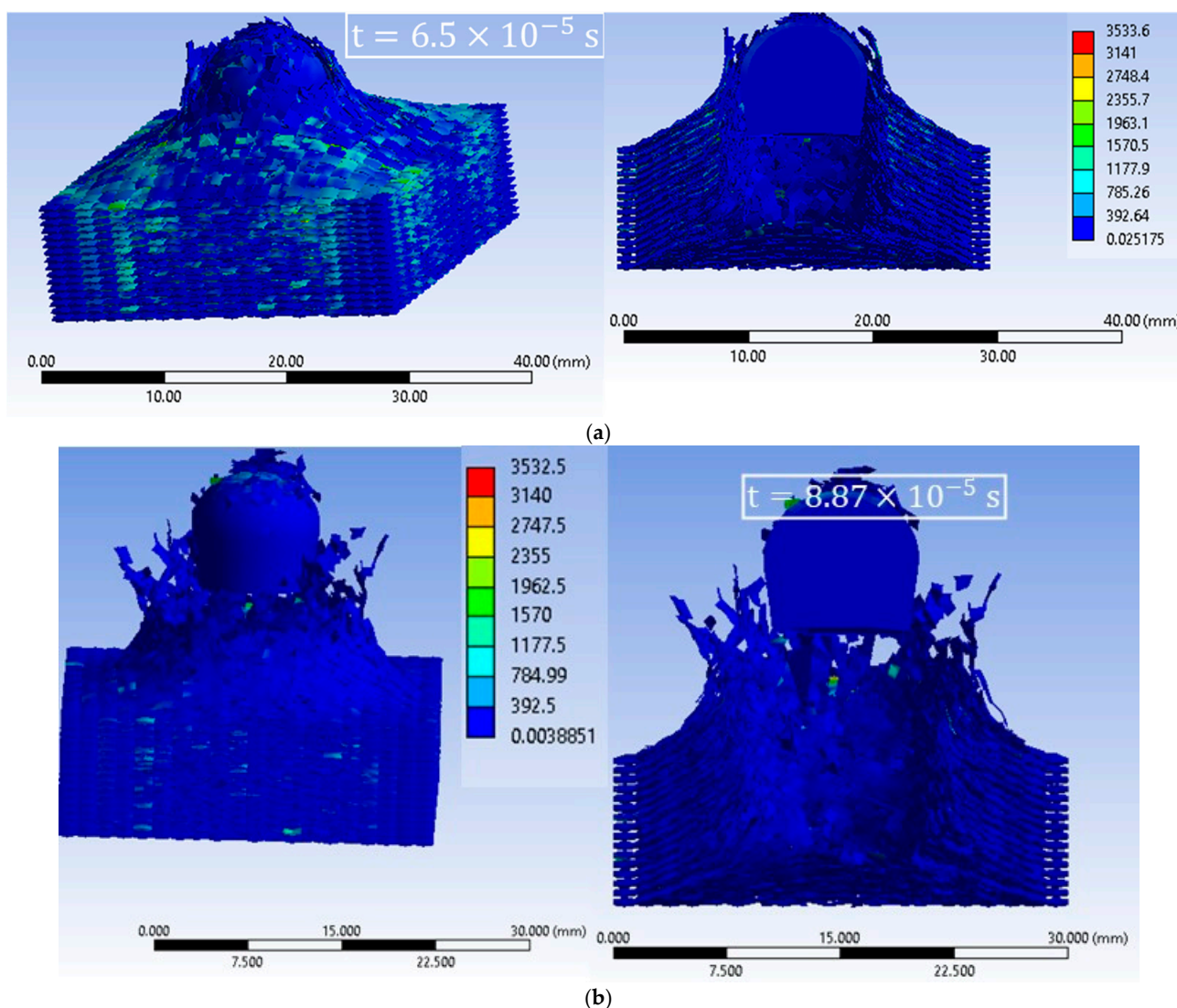


Figure 4. Equivalent stress distribution: (a) side view and sectional view at time $t = 6.5 \times 10^{-5}$ s; (b) side view and sectional view at time $t = 8.87 \times 10^{-5}$ s.

This analysis emphasizes how the plain weave structure contributes to the absorption and redistribution of the kinetic energy of the projectile. The interaction between the individual yarns, which are tensioned and deformed under the action of dynamic forces, causes stress propagation in the areas adjacent to the impact. This propagation facilitates energy dissipation and, in combination with the specific strength of the aramid fibers, leads to a complex mechanical response.

Visible fragments on the projectile nose indicate that the aramid fibers failed locally, but their high toughness characteristic allowed efficient energy dissipation before complete rupture. This validates the simulated behavior of the 16-layered panel and supports that the layered architecture and the chosen materials contribute significantly to the ballistic performance of the structure.

In both the numerical simulation and experimental results from [54], the panel is completely penetrated by the projectile. This behavior is due to the propagation of stress waves through the fabric and the ability of the projectile to generate a deformation large enough to tear the fabric layers. In the numerical simulation, it was observed that all layers of the fabric were completely penetrated, and at the end of the simulation, the projectile exited through the back of the panel. In the test experiments of [54], complete perforation of the panels occurs under similar conditions when the kinetic energy of the projectile exceeds the energy absorbed by the material.

One aspect that is emphasized, both in the numerical simulations and in [54], is the contribution of the main threads (the threads in direct contact with the projectile) to the absorption of kinetic energy. In the numerical simulation, the main threads are the first to be subjected to high stress, either compressive or tensile, and are responsible for dissipating a significant part of the projectile energy. Stress waves propagate along these threads, and their contribution can be visualized by the von Mises stress concentrations in the impact zones.

An experimental study showed that the main wires in the impact zone absorbed the energy by elastic and plastic deformation until they broke. The contribution of the main wires in the penetration process is visible from the images in [54]

A common observation between the numerical model and the literature is that the main wires are the ones that break in the impact zone, while the secondary wires are less affected. In the numerical simulation, the wires in direct contact with the projectile are subjected to both compression and extreme stretching, leading to their breakage. At the end of the simulation, in the impact zone, the primary yarns are fragmented into several pieces, while the secondary yarns remain only deformed or show incomplete breakage.

In the test experiments in [54], the fabric shows the same behavior—the main yarns in the impact zone are the most affected, with visible fragments around the penetration hole. Secondary yarns, further away from the projectile trajectory, contribute less to the energy absorption process and remain relatively intact.

The similarities observed between the numerical simulation and the experimental results described in the literature indicate a solid validation of the model. The complete penetration of the panel confirms that the numerical model can correctly reproduce the tissue damage mechanisms. The contribution of the main threads to kinetic energy absorption highlights the importance of detailed modeling of the thread properties and projectile–material interaction. The breakage of the main threads in the impact zone is a consistent result in both simulations and experimental tests, which supports the ability of the numerical model to faithfully reproduce the behavior of the fabric.

4. Results

The 16-layer model has been validated by comparing the simulation results with experimental data, thus ensuring that it correctly reflects the material behavior under normal impact conditions. After the validation of this model, reducing the number of layers is considered an efficient method to analyze the oblique impact, preserving the validity of the results without significantly increasing the computational complexity.

The analysis of the von Mises stress distribution is essential for understanding how materials behave upon ballistic impact in order to evaluate the deformation or failure mechanisms. In the context of simulating the impact of a projectile on an aramid fabric, the stress distribution during impact helps us to determine the zones of failure, indicating the areas where the material reaches or exceeds the yield strength (stress concentrators, red-colored areas), suggesting where the yarns or layers are most likely to break. This allows for the identification of areas of weakness where the fabric begins to fail under impact. Evaluating the stress distribution enables the identification of areas with excessive stress, allowing for improvements in the fabric's strength through modifications in fiber composition or structural adjustments to enhance ballistic impact protection.

The numerical simulation, with the projectile trajectory at 0° , normal impact, records, in the first moment of the simulation, the stressing of the first layer in the impact zone, affecting only the main wires (wires in direct contact with the projectile) (Figure 5). As the projectile advances, the main wires are stressed along their entire length. At the same time, as the projectile advances, the secondary wires (wires that are not in direct contact with the projectile) are also stressed. From the time moment $t = 5 \times 10^{-6}$ s, the cone starts to form on the back face of the target. The yarns are compressed by the projectile in the impact zone at the beginning of the simulation, which leads to a compressive breakage. With the advancement of the projectile through the target panel, the wires are stretched until they break. Yarn breakage in the impact zone is in the form of fragments that are also visible on the tip of the projectile. When the projectile perforates the fabric, the yarns are pushed to the side, creating a twist in the transverse direction. Before being broken, the analyzed wire is compressed and stretched. It is broken into two points in the impact zone. The bending in the transverse direction is generated by the projectile advancing through the panel, which also causes several fragments to break in that area. At the end of the simulation, the wire is broken to one side near the embedding zone. The von Mises stress recorded at the end of the simulation on this analyzed thread is 22% of the yield strength of the wire.

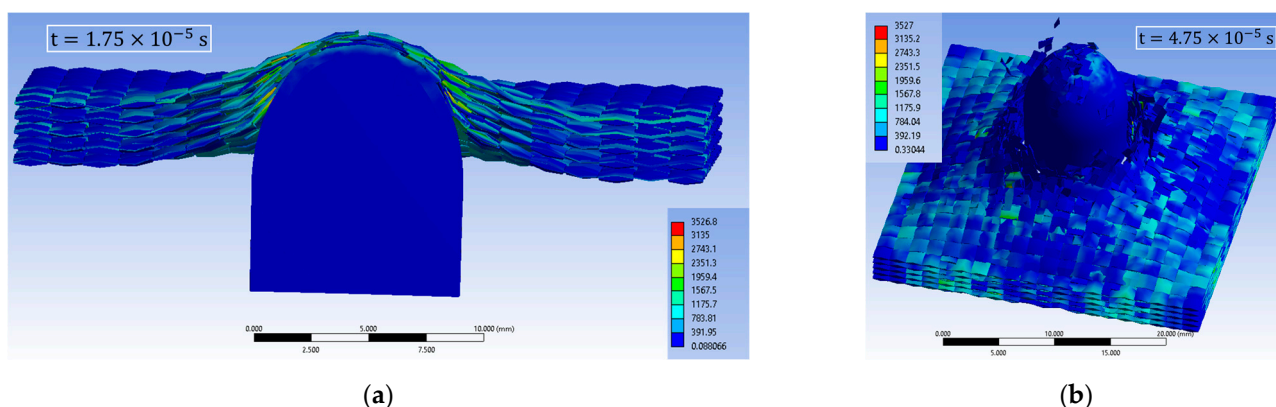


Figure 5. Equivalent stress distribution and mode of fabric destruction (the projectile trajectory at 0° , normal impact): (a) section in the middle; (b) side view of the perforated model.

Qian et al. [52], in their study, mention that the stress distribution mainly occurs along the main wires [52]. The main wires instantaneously transmit the stress waves to the edges in the longitudinal direction of the wires. The projectile pushes the main wires away from the direction of impact, facilitating penetration of the material due to the increased movement between the wires. This may elucidate the fact that the energy absorption capacity fluctuates with the variations in the fabric, as the yarns are significantly compressed and forced to move.

At the first moment of impact, in the simulation with the projectile trajectory oriented at 10° , the wires in the impact zone are observed to be stressed (Figure 6). In the second moment of the simulation, the stress waves expand, and the maximum stress increases by 27 MPa compared to the first moment. From the beginning of the simulation, the fabric layers are subjected to the compression exerted by the projectile. At time moment $t = 5 \times 10^{-6}$ s, the main wire is stressed to the edge. At the next moment, the wires that are in contact with the projectile on the first layer break due to compression. As the projectile advances, stress waves also become visible on the secondary wires. At time moment $t = 7.5 \times 10^{-6}$ s, the cone begins to form on the back face of the target. At time moment $t = 1.75 \times 10^{-5}$ s, all layers are broken. At the end of the impact, fragments of broken wires are visible on the nose of the projectile. The laminated panels are damaged in and around the impact zone, and the wires are pushed laterally, showing bending in the transverse direction. At the first moment of the simulation, the analyzed main wire shows a slight compression in the impact zone. At time moment $t = 5 \times 10^{-6}$ s, the wire is both compressed and stretched, showing small fragments breaking away from the impact zone. Complete breakage of this thread becomes visible at time moment $t = 1 \times 10^{-5}$ s. This breakage is not symmetric, with fragments of the wire being broken in the impact zone, as well as fragmentation of a part of the wire after it has been broken in the central zone.

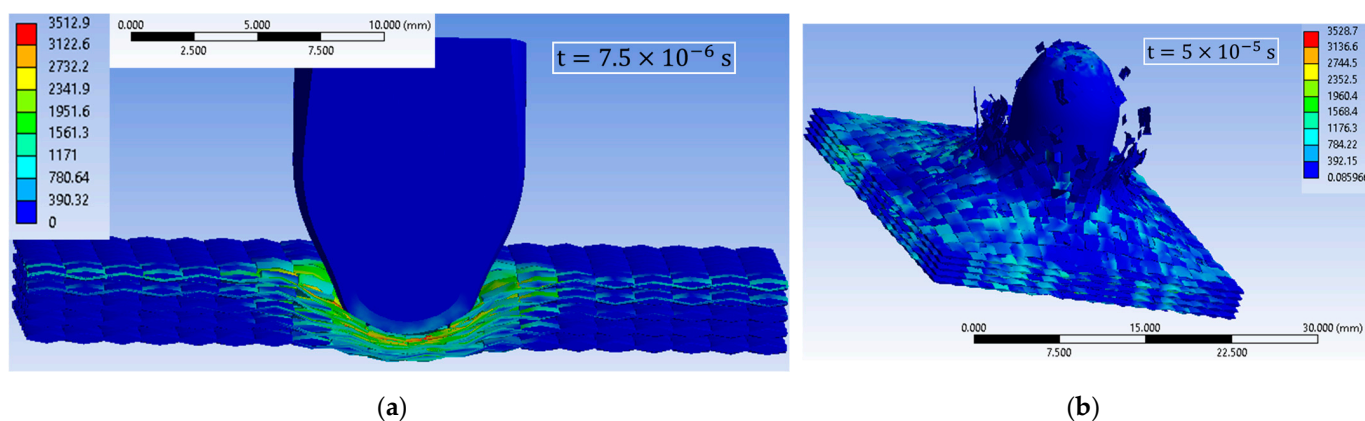


Figure 6. Equivalent stress distribution and mode of fabric destruction (the projectile trajectory oriented at 10°): (a) section in the middle; (b) side view of the perforated model.

The numerical simulation, with the projectile trajectory at 20° , shows at the time moment $t = 5 \times 10^{-6}$ s, a non-uniform equivalent stress distribution (Figure 7). The main wires are stressed from the impact zone to the end, but only on the inclined side of the projectile. At the next time, $t = 7.5 \times 10^{-6}$ s, there is a stressing of the wires along their entire length in the warp direction, while the wires in the weft direction remain stressed only in the impact zone to the end, on the side where the projectile is inclined at 20° , increasing only the number of affected wires. The transverse stress waves increase as the projectile perforates the fabric. Yarn compression is also present in this case. The yarns are compressed from the first moments of impact and break as the projectile advances. The main yarn being analyzed, in the direction of the weft, is compressed at the first moment of the simulation and is damaged at the next moment. This breakage is caused by compression. As the projectile advances, the wire also undergoes a tensile/stretch break in the projectile's inclination zone.

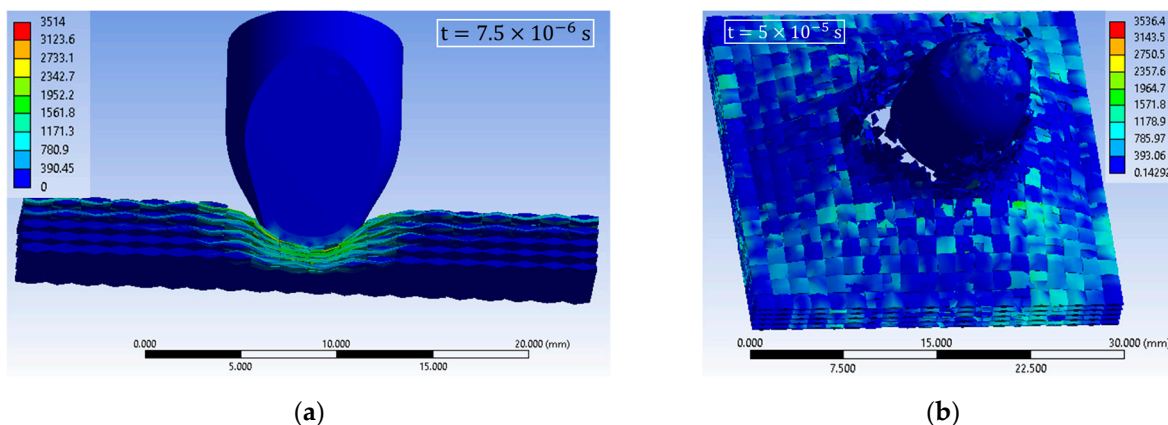


Figure 7. Equivalent stress distribution and mode of fabric destruction (the projectile trajectory at 20°): (a) section in the middle; (b) side view of the perforated model.

The numerical simulation, with the projectile trajectory set to 30°, shows stress waves in the impact zone at the simulation’s initial moment. At time moment $t = 5 \times 10^{-6}$ s, the tension of the wires is observed from the weft direction of the impact zone to the end, where the projectile is inclined. The next moment, $t = 7.5 \times 10^{-6}$ s, records the stressing of the wires in the warp direction in the longitudinal direction. At this time moment, the cone formation on the back face also starts. Starting at time moment $t = 2 \times 10^{-5}$ s, the projectile starts to damage all the layers and exit the fabric. The last moment of the simulation shows how the yarns are pushed sideways by the projectile, showing a longitudinal bending (the yarns in the weft direction) and a transverse bending (the yarns in the warp direction). The weft-direction yarn analyzed is partially broken at time $t = 5 \times 10^{-6}$ s, due to the compression exerted by the projectile. The next moment records its complete breakage. As the projectile perforates the fabric, fragments of the wire are broken, especially from the right side, while the left side shows a strong bending in the transverse direction due to the projectile trajectory oriented at 30°, accompanied by significant stretching (Figure 8).

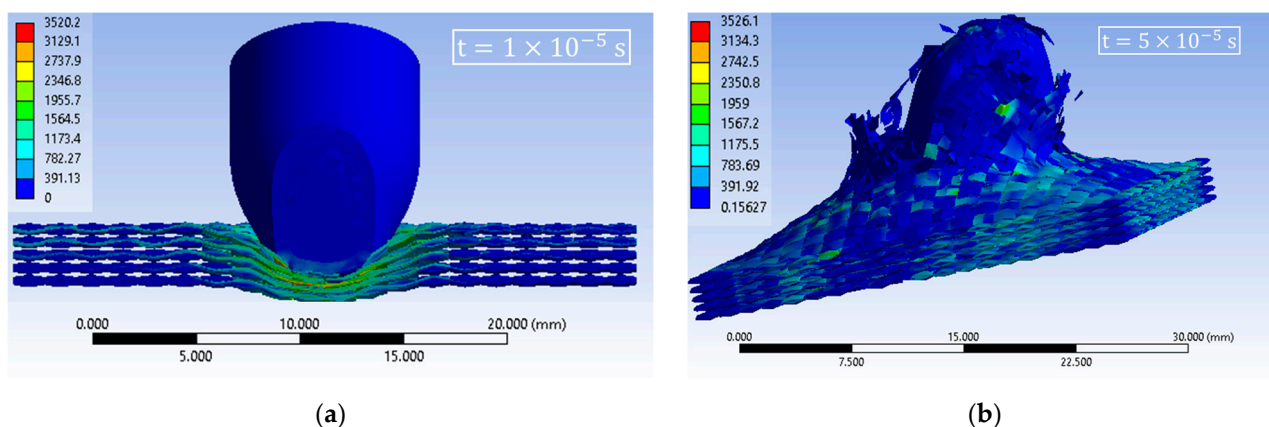


Figure 8. Equivalent stress distribution and mode of fabric destruction (the projectile trajectory set to 30°): (a) section in the middle; (b) side view of the perforated model.

The numerical simulation, with the projectile trajectory at 40°, records, in the first moment of the simulation, a maximum stress of 3482.4 MPa, a value below the yield limit. This first moment does not show any broken wires but only stressed wires in the impact zone. In the second moment of the simulation, $t = 5 \times 10^{-6}$ s, stress concentrators are observed on the edges of the wires in the impact zone, where the stress exceeds the yield stress of the wire, reaching a value of 3520 MPa. The main wires in the weft

direction are stressed all the way to their ends on the left side. At the next time moment, $t = 7.5 \times 10^{-6}$ s, stress waves are recorded along the entire length of the main wires in the warp direction. This moment also marks the beginning of the cone formation on the back face. At time moment $t = 1 \times 10^{-5}$ s, the breakage of the first layer is observed, a breakage caused by the compression of the material layer. At time moment $t = 2 \times 10^{-5}$ s, stress concentrators appear on the back face of the panel, with values around 3530 MPa. These stress concentrators indicate that, in those areas, the wires are susceptible to breakage. The wire breakage is not symmetrical; the wires on the left side of the projectile are broken, while the wires in the warp and weft directions on the right side are twisted in both transverse and longitudinal directions (Figure 9). The weft-direction wire analyzed shows, on the back face, an area with a stress concentrator of 3334.8 MPa, which is below the yield strength of the wire. This zone detaches from the wire at the second time instant of the simulation $t = 5 \times 10^{-6}$ s. At this moment, stress concentrators are also observed in the impact zone, indicating that at the next time instant, $t = 7.5 \times 10^{-6}$ s, the wire will undergo breakage. The last moment of the simulation shows that several fragments were broken from the wire, caused by bending in the transverse direction and stretching during the simulation.

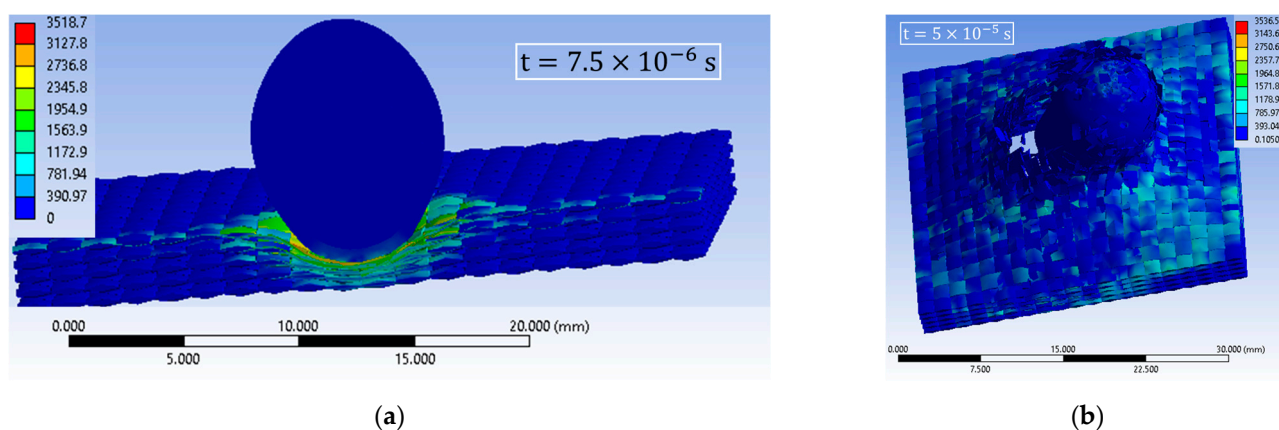


Figure 9. Equivalent stress distribution and mode of fabric destruction (the projectile trajectory at 40°): (a) section in the middle; (b) side view of the perforated model.

The first moment of the simulation, with the projectile trajectory oriented at 50° , records a maximum von Mises stress value of 2479.9 MPa, which is 71% of the yield strength of the wire. At time moment $t = 7.5 \times 10^{-6}$ s, higher von Mises stress values are observed at the ends of the wires in the impact zone. Wire breakage by compression becomes evident at time moment $t = 1 \times 10^{-5}$ s. Stress waves on the back face of the panel are visible starting at time moment $t = 1 \times 10^{-5}$ s. At time moment $t = 2.25 \times 10^{-5}$ s, areas of maximum von Mises stress values are recorded on the back face of the panel in the impact zone. The main analyzed wire, at the first time of the simulation, records a stress value of 1593.3 MPa, representing 46% of the yield strength of the wire. At this time moment, a stress concentrator zone is observed on the back face of the wire. The next time moment, $t = 5 \times 10^{-6}$ s, shows two areas with stress concentrators at the edges of the wire. At time moment $t = 5 \times 10^{-6}$ s, a partial wire break is observed, along with stress concentrators across the width of the wire in the impact zone. The complete wire breakage is recorded at time moment $t = 1 \times 10^{-5}$ s. During the simulation, several fragments of the wire are broken, which are caused by the stretching and transverse bending of the wire (Figure 10).

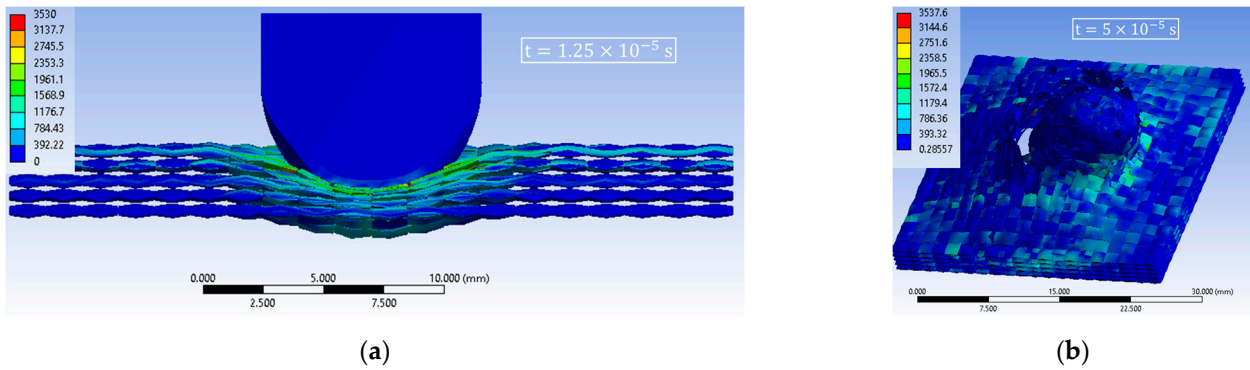


Figure 10. Equivalent stress distribution and mode of fabric destruction (the projectile trajectory oriented at 50°): (a) section in the middle; (b) side view of the perforated model.

The numerical simulation, with the projectile trajectory at 60°, records a von Mises stress value of 2011.4 MPa, representing 57% of the yield strength of the wire at the first moment of the simulation. At time moment $t = 7.5 \times 10^{-6}$ s, several areas of stress concentrators appear in the impact zone. At time moment $t = 1.25 \times 10^{-5}$ s, stress waves are visible on the back face of the panel in the impact zone. The projectile starts to push the wires of the first layer upwards due to the 60° impact trajectory, starting at time moment $t = 1.75 \times 10^{-5}$ s. In the following moments of the simulation, the other layers are also pushed. More wires are broken because the impact area is larger due to the projectile trajectory at 60°. The main analyzed wire registers a von Mises stress value of 1751.4 MPa, representing 50% of the yield strength of the wire. An area of stress concentrators is visible on the back face of the wire in the impact zone. The wire is both compressed and stretched, breaking at time moment $t = 1.25 \times 10^{-5}$ s. The wire breaks into several fragments due to stretching and bending in the left side area (Figure 11).

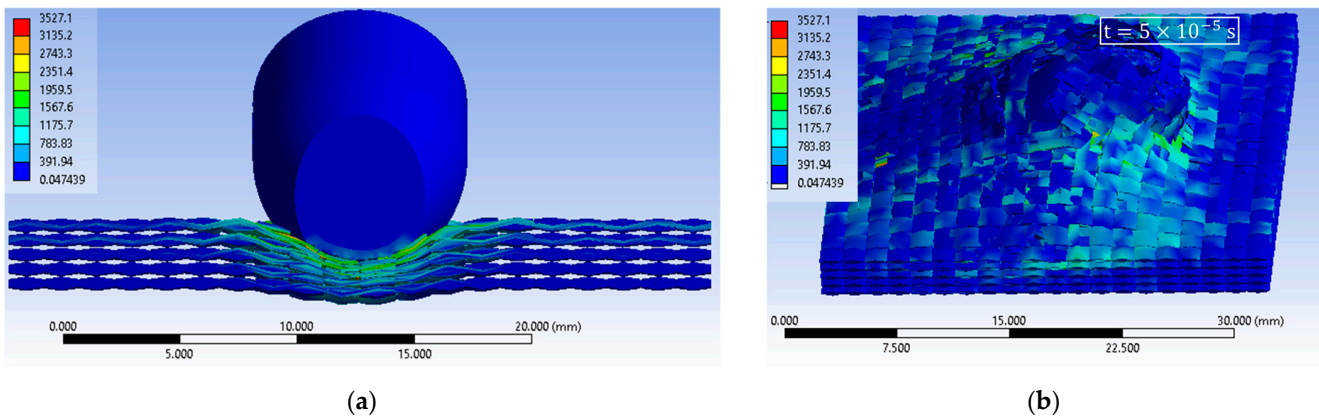


Figure 11. Equivalent stress distribution and mode of fabric destruction (the projectile trajectory at 60°): (a) section in the middle; (b) side view of the perforated model.

At the first moment of impact, no wire is touched in the case of the numerical simulation, with the projectile trajectory at 70°. The next moment records a very small stressed area. As the projectile advances through the fabric, the stressed area increases. At the time moment, stress waves are present on the wires in the warp direction, wires that contact the side of the projectile’s jacket (Figure 12). Starting at the time moment $t = 2 \times 10^{-5}$ s, the projectile pushes the layers upward. The area deformed by the projectile is very large because the projectile, as it advances, destroys the yarns with the lateral side, as well. The casing of the projectile is deformed around contact with the yarns. At the final time moment $t = 5 \times 10^{-5}$ s, the projectile failed to perforate all the layers, and a simulation with a longer

time is needed to penetrate the fabric. In this case, the fabric shows better impact resistance. The analyzed weft-direction yarn in the first three times is not tensioned. At time moment $t = 1 \times 10^{-5}$ s, the value of the maximum von Mises stress is 104 MPa, representing 3% of the yield strength of the yarn. The time moment $t = 2.25 \times 10^{-5}$ s records the partial rupture of this wire in the middle regions. The next time instant, time $t = 2.5 \times 10^{-5}$ s of the simulation records the splitting of the wire.

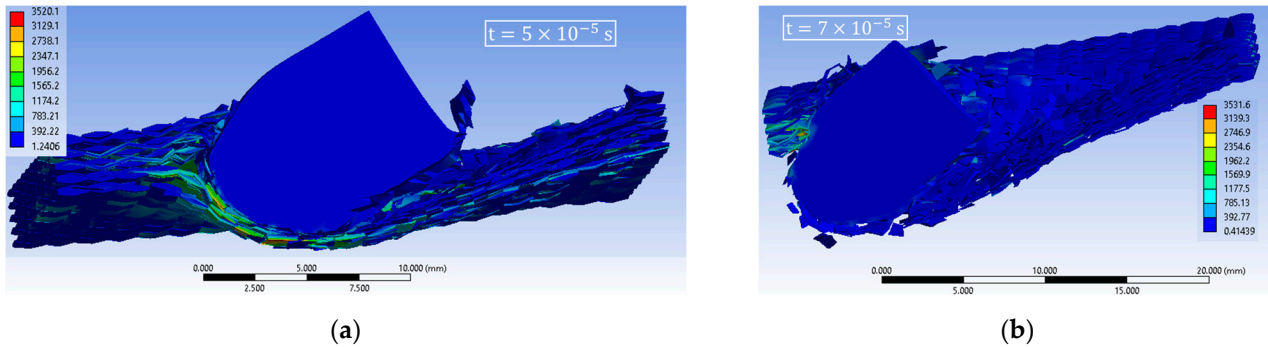


Figure 12. Equivalent stress distribution and mode of fabric destruction (the projectile trajectory at 70°): (a) section in the middle; (b) side view of the perforated model.

Table 2 provides the components of the initial impact velocity obtained with the above formulas and the velocities from Ansys. Table 3 provides the projectile velocities at the end of the numerical simulation, expressed as a percentage of the initial impact velocity. Table 4 provides the projectile velocities at the end of the numerical simulation, expressed as a percentage of the initial velocity in the x and y directions, respectively, inferred from the numerical simulation. Table 5 provides the projectile velocities at the end of the numerical simulation, expressed as a percentage of the initial velocity in the x and y directions, respectively, calculated analytically.

Table 2. Velocity components in the x and y directions.

Model	V_i [m/s]	V_x [m/s]	V_y [m/s]	V_x [m/s] Ansys	V_y [m/s] Ansys
0°	400	0	400	0	400
10°	400	69.46	393.92	0	400
20°	400	136.81	375.88	136.81	375.88
30°	400	200	346.41	200	346.41
40°	400	257.12	306.42	257.12	306.42
50°	400	306.42	257.12	306.42	257.12
60°	400	346.41	200	346.41	200
70°	400	375.88	136.81	375.88	136.81

V_i —the initial impact velocity; V_x —x-axis velocity component; V_y —y-axis velocity component.

Table 3. Projectile velocities at the end of the numerical simulation expressed as a percentage of the initial impact velocity.

Model	V_i [m/s]	V_{xf} [m/s]	V_{yf} [m/s]	$\Delta V_x = \frac{V_{xf} \cdot 100}{V_i}$ [%]	$\Delta V_y = \frac{V_{yf} \cdot 100}{V_i}$ [%]
0°	400	63.26	243	15.82	60.75
10°	400	39.772	32.351	9.94	8.09
20°	400	148.23	33.68	37.06	8.42
30°	400	194.08	75.118	48.52	18.78
40°	400	270.27	61.445	67.57	15.36
50°	400	296.66	20.385	74.17	5.10
60°	400	108.43	9.291	27.11	2.32
70°	400	453.23	253.53	113.31	63.38

V_i —the initial impact velocity; V_{xf} —x-axis velocity component at the end of the numerical simulation; V_{yf} —y-axis velocity component at the end of the numerical simulation.

Table 4. The projectile velocities at the end of the numerical simulation expressed as a percentage of the initial velocity in the x and y directions, respectively, in Ansys.

Model	V_x [m/s] Ansys	V_y [m/s] Ansys	V_{xf} [m/s]	V_{yf} [m/s]	$\Delta V_x = \frac{V_{xf} \cdot 100}{V_x}$ [%]	$\Delta V_y = \frac{V_{yf} \cdot 100}{V_y}$ [%]
0°	0	400	63.26	243	-	60.75
10°	0	400	39.772	32.351	-	8.09
20°	136.81	375.88	148.23	33.68	108.35	8.96
30°	200	346.41	194.08	75.118	97.04	21.68
40°	257.12	306.42	270.27	61.445	105.11	20.05
50°	306.42	257.12	296.66	20.385	96.81	7.93
60°	346.41	200	108.43	9.291	31.30	4.65
70°	375.88	136.81	453.23	253.53	120.58	185.32

V_x —x-axis velocity component; V_{xf} —x-axis velocity component at the end of the numerical simulation; V_{yf} —y-axis velocity component at the end of the numerical simulation.

Table 5. The projectile velocities at the end of the numerical simulation expressed as a percentage of the initial velocity in the x and y directions, respectively, and calculated analytically.

Model	V_x [m/s]	V_y [m/s]	V_{xf} [m/s]	V_{yf} [m/s]	$\Delta V_x = \frac{V_{xf} \cdot 100}{V_x}$ [%]	$\Delta V_y = \frac{V_{yf} \cdot 100}{V_y}$ [%]
0°	0	400	63.26	243	0	60.75
10°	69.46	393.92	39.772	32.31	57.26	8.21
20°	136.81	375.88	148.23	33.68	108.35	8.96
30°	200	346.41	194.08	75.11	97.04	21.68
40°	257.12	306.42	270.27	61.44	105.11	20.05
50°	306.42	257.12	296.66	20.38	96.81	7.93
60°	346.41	200	108.43	9.29	31.30	4.65
70°	375.88	136.81	453.23	253.53	120.58	185.32

V_x —x-axis velocity component; V_{xf} —x-axis velocity component at the end of the numerical simulation; V_{yf} —y-axis velocity component at the end of the numerical simulation.

In Figure 13, the equivalent stress distribution is given on the analyzed main wire and projectile velocities as a function of time.

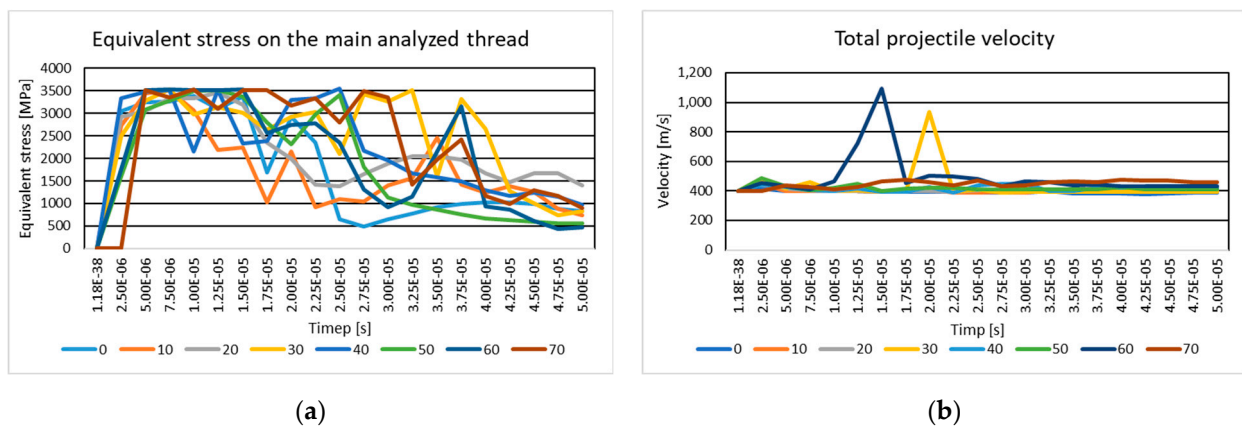


Figure 13. Cont.

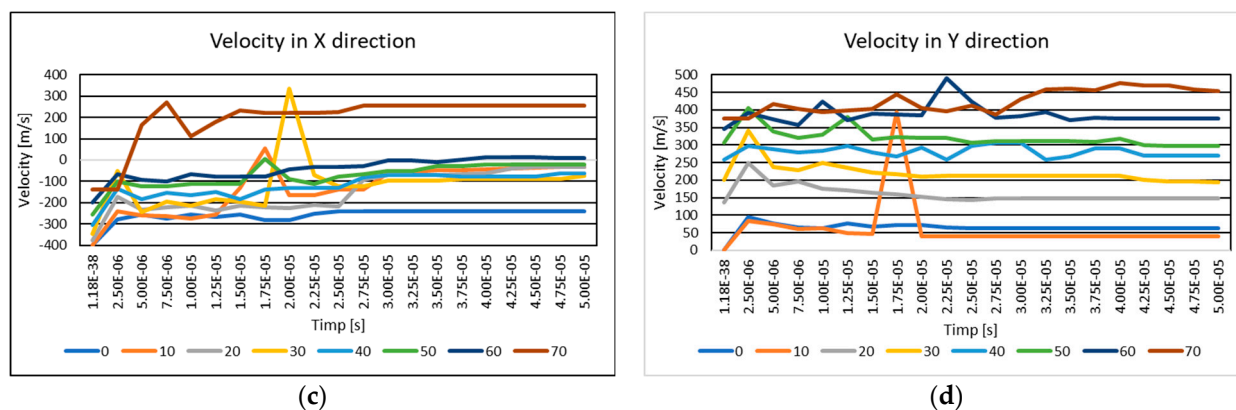


Figure 13. (a) Distribution of von Mises stress on the main analyzed wire; (b) total projectile velocity as a function of time; (c) x-axis component of projectile velocity during impact; (d) x-axis component of projectile velocity during impact.

5. Discussion

At small angles ($10\text{--}20^\circ$), the longitudinal component of velocity is dominant, which means that the projectile directly transfers kinetic energy in the normal direction of the tissue surface. This facilitates a rapid transfer of energy and produces sudden stressing of the threads in the central impact zone. The main threads are the first to fail, as they bear the greatest stress. Perforation time is short, and perforation occurs almost exclusively by tensile mechanisms. The simulations confirm that at low angles, the threads in the impact region are the most stressed and are mainly responsible for energy absorption.

At angles of 30° and 40° , the longitudinal and transverse components of the velocity become more balanced, leading to an increase in the contact area between the projectile and the fabric. The transverse component of the velocity, which is larger compared to small angles, plays an important role in slightly deflecting the projectile trajectory and generating lateral forces that progressively tension the yarns. This results in a more even stress distribution, delaying yarn breakage and allowing the fabric to dissipate more energy. The breakage mechanisms remain dominated by tension and shear, but the more uniform stress distribution and extensive interactions with the fabric increase the time required for perforation. The deviation of the projectile from its initial trajectory reduces the efficiency of energy transfer directly to the center area, redistributing stress to the adjacent threads and thus contributing to the improved ballistic performance of the panel.

At an angle of 50° , the transverse component of velocity becomes predominant, leading to a more complex interaction between the projectile and the layered fabric. The projectile tends to push the yarns laterally, which causes a more extensive deformation of the fabric prior to tearing. This lateral deformation contributes to distributing the stress over a larger area, reducing its concentration in the center points and favoring energy dissipation through the yarn network. The simulations show a greater loss of kinetic energy of the projectile as a result of the increased interactions with the fabric. The projectile encounters greater resistance due to the stretching and lateral displacement mechanisms of the yarns. This leads to a reduction in its penetration velocity and a longer perforation time compared to the lower angles. The predominant breakage mechanisms include tensile and shear, but the contribution of lateral interactions and extensive deformation enhances panel strength. The failure of the main yarns in the impact zone, observed in both simulations and experimental tests, emphasizes their critical role in energy absorption and in determining the overall performance of the fabric.

At the 60° angle, the transverse component of velocity becomes dominant, resulting in significant projectile–tissue interactions. The projectile transfers kinetic energy to the

threads in the impact zone, and the generated stress propagates over a large area, including the lateral regions of the fabric. This contributes to a more efficient dissipation of kinetic energy throughout the structure. Fabric deformation includes both stretching and lateral displacement, reflecting the complex behavior of the material. The upper layers are most stressed, while the lower layers remain relatively intact for a longer period of time. The puncture time is significantly higher compared to the lower angles, indicating increased panel strength at this angle. The simulations confirm these results, emphasizing the ability of the fabric to dissipate energy, which delays the perforation process.

At an angle of 70° , the transverse component of velocity becomes dominant, and the projectile encounters significant opposition from the tissue. Kinetic energy is transferred less efficiently in the central impact region due to the maximum deviation of the projectile. In this area, yarn breakage is a slower process and involves complex mechanisms, such as traction, shear, and lateral stretching, which allow better energy dissipation. The simulations show that at this angle, the projectile is able to fully penetrate the panel, but a longer simulation time was needed to observe this. This suggests an optimal ballistic performance of the fabric at high angles, where the fabric resists significantly more and allows efficient energy dissipation. This observation confirms the increased resistance of the fabric to oblique impacts, especially at high-impact angles.

The initial 16-layer model was validated by comparison with a literature paper, demonstrating good agreement between the simulation results and experimental data. This confirmed the accuracy of the model in ballistic simulations; in particular, in terms of energy transfer and thread-breakage mechanisms. To reduce computational time and allow faster simulations, the number of layers was reduced to five while still maintaining the essential material behaviors. This compromise allowed us to obtain valid results in agreement with those obtained for the 16-layer model, demonstrating that the 5-layer model is sufficiently representative for the study of the ballistic behavior of the fabric.

The impact at different angles (10° , 20° , 30° , 40° , 50° , 60° , and 70°) showed how the fabric responds depending on the direction of impact. At low angles, the impact is more effective in penetrating the fabric quickly, while at high angles, the projectile encounters greater resistance, leading to improved ballistic performance. At high angles, the thread-breaking mechanisms are more complex and include traction, shearing, and lateral stretching, which allows better energy dissipation.

6. Conclusions

The numerical analysis in this study is modeled at the thread level. The modeled fabric is a plain weave, modeled with the dimensions of a real fabric, in order to provide results that can help in obtaining protection systems.

The analysis of the impact between the target and the projectile at different impact angles, from 0° to 70° with a 10° increment, is based on the equivalent stress distribution to determine how the projectile trajectory influences the distribution of the stress waves and the way the fabric is damaged. These results are valuable for the design of more effective ballistic protection equipment that can be adapted to withstand a wide range of angles and conditions.

The projectile trajectory is one of the factors influencing ballistic impact performance. As the projectile trajectory increased, the area damaged increased. When the projectile trajectory is between 30° – 70° , the layers are damaged with the tip of the projectile as well as the body of the projectile, which also results in an increased destroyed area. As the projectile's trajectory increases, the fabric provides more resistance.

The cone formation on the back face is visible until the impact of the projectile with the projectile trajectory at 60°. In the simulated case, with the projectile trajectory at 70 degrees, the cone formation is visible halfway as the projectile makes its way through the layers.

The interaction of the wires at their intersection sites induces the propagation of longitudinal and transverse waves from the main wires into adjacent wires, resulting in a pyramid-shaped transverse deformation. After the longitudinal tension wave reaches the fixed edge of the panel, the longitudinal tensile wave from the main weft wire is reflected as a tensile wave, which then interacts with the transverse wave in the wire, resulting in an increased transverse wave velocity. The transverse displacement of the layered panel after oblique impact differs from that observed during normal impact. The panel exhibits asymmetry behavior along the main strands, which intensifies with obliquity.

In the numerical simulations in this paper, the following mechanisms contributing to energy absorption during impact were identified and were also identified in the literature [2,19,52,56–59]:

- Compression of the wires under the projectile, in the first moments of the simulation, in the impact zone;
- Cone formation on the back face of the last layer;
- Tension waves on the main wires at the beginning of the impact, propagating to the last and secondary wires;
- Breaking of the main wires by stretching and bending;
- Breaking of the secondary wires by bending.

Author Contributions: Conceptualization, L.T. and C.M.; methodology, L.T. and C.M.; software, L.T. and C.M.; formal analysis, L.T. and C.M.; investigation, L.T. and C.M.; resources, L.T. and C.M.; data curation, L.T.; writing—original draft preparation, L.T.; writing—review and editing, C.M.; visualization, L.T.; supervision, C.M. All authors have read and agreed to the published version of the manuscript.

Funding: This research received no external funding.

Data Availability Statement: Data are contained within the article.

Conflicts of Interest: The authors declare no conflicts of interest.

References

1. Pai, A.; Kini, C.; Shenoy, S. Development of materials and structures for shielding applications against Blast and Ballistic impact: A Detailed Review. *Thin-Walled Struct.* **2022**, *179*, 10966. [[CrossRef](#)]
2. Abtew, M.A.; Boussu, F.; Bruniaux, P.; Loghin, C.; Cristian, I. Ballistic impact mechanisms—A review on textiles and fibre-reinforced composites impact responses. *Compos. Struct.* **2019**, *223*, 110966. [[CrossRef](#)]
3. Bezerra, W.B.A.; Lazarus, B.S.; Costa, U.O.; Figueiredo, A.B.-H.S.; Lima, É.P., Jr.; Luz, F.S.; Monteiro, S.N. Energy Absorption and Ballistic Performance of Epoxy Composite Reinforced with Arapaima Scales. *Polymers* **2023**, *15*, 1614. [[CrossRef](#)]
4. Shim, V.P.W.; Guo, Y.B.; Tan, V.B.C. Response of woven and laminated high-strength fabric to oblique impact. *Int. J. Impact Eng.* **2012**, *48*, 87–97. [[CrossRef](#)]
5. Xie, J.; Pan, H.; Feng, Z.; Zhen, T.; Jiang, C.; Jiang, Y.; Li, X. Experimental study on the blast resistance of polyurea-coated aramid fabrics. *Int. J. Impact Eng.* **2024**, *195*, 105120. [[CrossRef](#)]
6. Pinkos, J.; Stempien, Z.; Małkowska, M. Numerical and experimental analysis of ballistic performance in hybrid soft armours composed of para-aramid triaxial and biaxial woven fabrics. *AUTEX Res. J.* **2024**, *24*, 20230022. [[CrossRef](#)]
7. Ji, H.; Wang, X.; Tang, N.; Li, B.; Li, Z.; Geng, X.; Lu, T.J. Ballistic perforation of aramid laminates: Projectile nose shape sensitivity. *Compos. Struct.* **2024**, *330*, 117807. [[CrossRef](#)]
8. Zheng, X.; Wu, H.; Li, X.; Hu, Q.; Yan, K.; Qi, S.; Yuan, M. Experimental and numerical study on ballistic response of stitched aramid woven fabrics under normal and oblique dynamic impact. *Thin-Walled Struct.* **2024**, *205*, 112424. [[CrossRef](#)]
9. Langston, T. An analytical model for the ballistic performance of ultra-high molecular weight polyethylene composites. *Compos. Struct.* **2017**, *179*, 245–257. [[CrossRef](#)]

10. Ma, D.; Scazzosi, R.; Manes, A. Modeling approaches for ballistic simulations of composite materials: Analytical model vs. finite element method. *Compos. Sci. Technol.* **2024**, *248*, 110461. [[CrossRef](#)]
11. Libin, T.; Akash, K.A.; Sivagangai, T. Experimental, analytical, and numerical study of ballistic limit and energy absorption of thin aluminium plate against projectile impact. *Mater. Today Proc.* **2024**, *in press*. [[CrossRef](#)]
12. Ding, L.; Gu, X.; Shen, P.; Kong, X. Ballistic Limit of UHMWPE Composite Armor under Impact of Ogive-Nose Projectile. *Polymers* **2022**, *14*, 4866. [[CrossRef](#)] [[PubMed](#)]
13. Alkhatib, F.; Mahdi, E.; Dean, A. Design and Evaluation of Hybrid Composite Plates for Ballistic Protection: Experimental and Numerical Investigations. *Polymers* **2021**, *13*, 1450. [[CrossRef](#)] [[PubMed](#)]
14. Peinado, J.; Jiao-Wang, L.; Olmedo, Á.; Santiuste, C. Utilizarea rețelelor neuronale artificiale pentru a optimiza secvența de stivuire în protecțiile UHMWPE. *Polymers* **2021**, *13*, 1012. [[CrossRef](#)]
15. Zhou, Y.; Gong, X.; Zhang, S.; Xu, A. A numerical investigation into the influence of layer space on panel ballistic performance. *Fibers Polym.* **2015**, *16*, 2663–2669. [[CrossRef](#)]
16. Ivañez, I.; Santiuste, C.; Barbero, E.; Sanchez-Saez, S. Numerical modelling of foam-cored sandwich plates under high-velocity impact. *Compos. Struct.* **2011**, *93*, 2392–2399. [[CrossRef](#)]
17. Nguyen, L.H.; Lässig, T.R.; Ryan, S.; Riedel, W.; Mouritz, A.P.; Orifici, A.C. Numerical Modelling of Ultra-High Molecular Weight Polyethylene Composite under Impact Loading. *Proc. Eng.* **2015**, *103*, 436–443. [[CrossRef](#)]
18. Xing, J.; Du, C.; He, X.; Zhao, Z.; Zhang, C.; Li, Y. Finite Element Study on the Impact Resistance of Laminated and Textile Composites. *Polymers* **2019**, *11*, 1798. [[CrossRef](#)]
19. Rajagopal, A.; Naik, N.K. Oblique ballistic impact behavior of composites. *Int. J. Damage Mech.* **2014**, *23*, 453–482. [[CrossRef](#)]
20. Zhang, C.; Zhu, Q.; Curiel-Sosa, J.L.; Bui, T.Q. Ballistic performance and damage simulation of fiber metal laminates under high-velocity oblique impact. *Int. J. Damage Mech.* **2020**, *29*, 1011–1034. [[CrossRef](#)]
21. Biswas, K.; Datta, D. Oblique impact on ceramic–composite armor system: A numerical study. *Proc. Inst. Mech. Eng. Part L J. Mater. Des. Appl.* **2024**, *238*, 1256–1267. [[CrossRef](#)]
22. Goda, I. Ballistic resistance and energy dissipation of woven-fabric composite targets: Insights on the effects of projectile shape and obliquity angle. *Def. Technol.* **2023**, *21*, 14–32. [[CrossRef](#)]
23. Iqbal, M.A.; Gupta, G.; Gupta, N.K. 3D numerical simulations of ductile targets subjected to oblique impact by sharp nosed projectiles. *Int. J. Solids Struct.* **2010**, *47*, 224–237. [[CrossRef](#)]
24. Nunes, S.G.; Scazzosi, R.; Manes, A.; Amico, S.C.; de Amorim Júnior, W.F.; Giglio, M. Influence of projectile and thickness on the ballistic behavior of aramid composites: Experimental and numerical study. *Int. J. Impact Eng.* **2019**, *132*, 103307. [[CrossRef](#)]
25. Liu, P.; Liu, Y.; Wang, Z.; Chen, J.; Zhang, H.; Huang, G. A design model of multi-layer modified aramid fabrics against fragment simulating projectiles and full metal jacketed bullets. *Int. J. Impact Eng.* **2024**, *191*, 104989. [[CrossRef](#)]
26. Pham, Q.H.; Ha-Minh, C.; Chu, T.L.; Kanit, T.; Imad, A. Numerical investigation of fibre failure mechanisms of one single Kevlar yarn under ballistic impact. *Int. J. Solids Struct.* **2022**, *239*, 111436. [[CrossRef](#)]
27. Droß, M.; Heyser, P.; Meschut, G.; Hürkamp, A.; Dröder, K. Fiber response to pin penetration in dry woven fabric using numerical analysis. *J. Adv. Join. Process.* **2022**, *5*, 100083. [[CrossRef](#)]
28. Nilakantan, G. Filament-level modeling of Kevlar KM2 yarns for ballistic impact studies. *Compos. Struct.* **2013**, *104*, 1–13. [[CrossRef](#)]
29. Sockalingam, S.; Gillespie, J.W., Jr.; Keefe, M. On the transverse compression response of Kevlar KM2 using fiber-level finite element model. *Int. J. Solids Struct.* **2014**, *51*, 2504–2517. [[CrossRef](#)]
30. MyNauticExpo. Available online: <https://pdf.nauticexpo.com/pdf/teijin-aramid-bv/ballistic-material-handbook/30430-74521.html> (accessed on 1 August 2024).
31. Zeng, X.S.; Tan, V.B.C.; Shim, V.P.W. Modelling inter-yarn friction in woven fabric armour. *Jurnalul Internațional Pentru Metode Numer. Ing.* **2006**, *66*, 1309–1330. [[CrossRef](#)]
32. Wang, Y.; Chen, X.; Young, R.; Kinloch, I. Finite element analysis of effect of inter-yarn friction on ballistic impact response of woven fabrics. *Compos. Struct.* **2016**, *135*, 8–16. [[CrossRef](#)]
33. Chu, Y.; Min, S.; Chen, X. Numerical study of inter-yarn friction on the failure of fabrics upon ballistic impacts. *Mater. Des.* **2017**, *115*, 299–316. [[CrossRef](#)]
34. Lim, C.T.; Shim, V.P.; Ng, Y.H. Finite-element modeling of the ballistic impact of fabric armor. *Int. J. Impact Eng.* **2004**, *28*, 13–31. [[CrossRef](#)]
35. Rao, M.; Duan, Y.; Keefe, M.; Powers, B.; Bogetti, T. Modeling the effects of yarn material properties and friction on the ballistic impact of a plain-weave fabric. *Compos. Struct.* **2009**, *89*, 556–566. [[CrossRef](#)]
36. Ballistic Materials Handbook Teijin Aramid and Ballistic Protection n.d. Available online: https://www.teijinaramid.com/wp-content/uploads/2019/11/TEIJ_Handbook_Ballistics_2019_DEF.pdf (accessed on 1 August 2024).
37. Bocian, M.; Pach, J.; Jamroziak, K.; Kosobudzki, M.; Polak, S.; Pyka, D.; Kurzawa, A.; Kurowski, J. Experimental and numerical analysis of aramid fiber laminates with DCPD resin matrix subjected to impact tests. *MATEC Web Conf.* **2017**, *112*, 4013. [[CrossRef](#)]

38. Yang, Y.; Chen, X. Influence of fabric architecture on energy absorption efficiency of soft armour panel under ballistic impact. *Compos. Struct.* **2019**, *224*, 111015. [[CrossRef](#)]
39. Chu, T.L.; Ha-Minh, C.; Imad, A. A numerical investigation of the influence of yarn mechanical and physical properties on the ballistic impact behavior of a Kevlar KM2[®] woven fabric. *Compos. Part B Eng.* **2016**, *95*, 144–154. [[CrossRef](#)]
40. Cheng, M.; Chen, W.; Weerasooriya, T. Mechanical properties of Kevlar[®] KM2 single fiber. *J. Eng. Mater. Technol.* **2005**, *127*, 197–203. [[CrossRef](#)]
41. Leal, A.A.; Deitzel, J.M.; Gillespie, J.W., Jr. Compressive strength analysis for high performance fibers with different modulus in tension and compression. *J. Compos. Mater.* **2009**, *43*, 661–674. [[CrossRef](#)]
42. Chawla, K.K.; Chawla, N. 1.1 Fibrous Reinforcements for Composites. In *Comprehensive Composite Materials II*; Beaumont, P.W.R., Zweben, C.H., Eds.; Elsevier: Amsterdam, The Netherlands, 2018; pp. 1–12. ISBN 9780081005347. [[CrossRef](#)]
43. Yang, Y.; Liu, Y.; Xue, S.; Sun, X. Multi-scale finite element modeling of ballistic impact onto woven fabric involving fiber bundles. *Compos. Struct.* **2021**, *267*, 113856. [[CrossRef](#)]
44. Bilisik, K. Two-dimensional (2D) fabrics and three-dimensional (3D) preforms for ballistic and stabbing protection: A review. *Text. Res. J.* **2017**, *87*, 2275–2304. [[CrossRef](#)]
45. Alaboodi, A.S.; Yusoff, N.B.; Alnasser, A.A. Modelling and simulation of three-roll bending process of bimetal Circular Billet. *IOP Conf. Ser. Mater. Sci. Eng.* **2019**, *697*, 012013. [[CrossRef](#)]
46. Yin, S.; Wang, X.F.; Li, W.Y.; Xu, B.P. Numerical investigation on effects of interactions between particles on coating formation in cold spraying. *J. Therm. Spray Technol.* **2009**, *18*, 686–693. [[CrossRef](#)]
47. Peroni, L.; Scapin, M.; Fichera, C.; Manes, A.; Giglio, M. Mechanical properties at high strain-rate of lead core and brass jacket of a NATO 7.62 mm ball bullet. *EPJ Web Conf.* **2012**, *26*, 01060. [[CrossRef](#)]
48. Johnson, G.R.; Cook, W.H. Fracture Characteristics of Three Metals Subjected to Various Strains, Strain Rates, Temperatures and Pressures. *Eng. Fract. Mech.* **1985**, *21*, 31–48. [[CrossRef](#)]
49. Forrestal, M.J.; Børvik, T.; Warren, T.L. Perforation of 7075-T651 Aluminum Armor Plates with 7.62 mm APM2 Bullets. *Exp. Mech.* **2010**, *50*, 1245–1251. [[CrossRef](#)]
50. Manes, A.; Serpellini, F.; Pagani, M.; Saponara, M.; Giglio, M. Perforation and penetration of aluminium target plates by armour piercing bullets. *Int. J. Impact Ing.* **2014**, *69*, 39–54. [[CrossRef](#)]
51. Børvik, T.; Dey, S.; Clausen, A.H. Perforation resistance of five different high-strength steel plates subjected to small-arms projectiles. *Int. J. Impact Ing.* **2009**, *36*, 948–964. [[CrossRef](#)]
52. Qian, X.; Zhou, Y.; Cai, L.; Pei, F.; Li, X. Computational simulation of the ballistic impact of fabrics using hybrid shell element. *J. Eng. Fibers Fabr.* **2020**, *15*, 1558925020973542. [[CrossRef](#)]
53. Doddamani, S.; Kulkarni, S.M.; Joladarashi, S.; TS, M.K.; Gurjar, A.K. Analysis of light weight natural fiber composites against ballistic impact: A review. *Int. J. Lightweight Mater. Manuf.* **2023**, *6*, 450–468. [[CrossRef](#)]
54. Chiper, T.L. Numerical and Experimental Study for Ballistic Protection Systems with Aramid Fibre Fabrics. Ph.D. Thesis, Dunarea de Jos University, Galati, Romania, 2023.
55. *NIJ Standard-0101.06*; Ballistic Resistance of Body Armor. U.S. Department of Justice Office of Justice Programs National Institute of Justice: Washington, DC, USA, 2008.
56. Dewangan, M.K.; Panigrahi, S.K. Factors influencing the ballistic impact mechanisms of textile composite materials: A review. *Polym. Adv. Technol.* **2021**, *32*, 1901–1923. [[CrossRef](#)]
57. Nair, N.S.; Kumar, C.V.S.; Naik, N.K. Ballistic impact performance of composite targets. *Mater. Des.* **2013**, *51*, 833–846. [[CrossRef](#)]
58. Naik, N.K.; Shrirao, P. Composite structures under ballistic impact. *Compos. Struct.* **2014**, *66*, 579–590. [[CrossRef](#)]
59. Chen, X.; Zhu, F.; Wells, G. An analytical model for ballistic impact on textile based body armour. *Compos. Part B Eng.* **2013**, *45*, 1508–1514. [[CrossRef](#)]

Disclaimer/Publisher’s Note: The statements, opinions and data contained in all publications are solely those of the individual author(s) and contributor(s) and not of MDPI and/or the editor(s). MDPI and/or the editor(s) disclaim responsibility for any injury to people or property resulting from any ideas, methods, instructions or products referred to in the content.